J. Fluid Mech. (2022), *vol*. 946, A15, doi:10.1017/jfm.2022.542

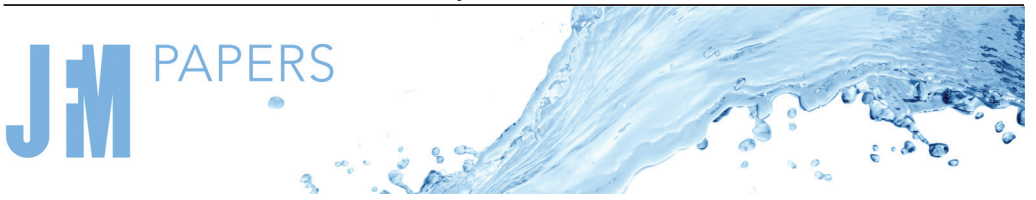

Elastic solid dynamics in a coupled oscillatory Couette flow system

Tejaswin Parthasarathy[1], **Yashraj Bhosale**[1] **and Mattia Gazzola**[1,2,3,†]

[1]Mechanical Sciences and Engineering, University of Illinois at Urbana-Champaign, Urbana, IL 61801, USA

[2]Carl R. Woese Institute for Genomic Biology, University of Illinois at Urbana-Champaign, Urbana, IL 61801, USA

[3]National Center for Supercomputing Applications, University of Illinois at Urbana-Champaign, Urbana, IL 61801, USA

(Received 28 December 2021; revised 29 April 2022; accepted 14 June 2022)

We report analytical solutions of a problem involving a visco-elastic solid material layer sandwiched between two fluid layers, in turn confined by two long planar walls that undergo oscillatory motion. The resulting system dynamics is rationalized, based on fluid viscosity and solid elasticity, via wave and boundary layer theory. This allows for physical interpretation of elasto-hydrodynamic coupling, potentially connecting to a broad set of biophysical phenomena and applications, from synovial joint mechanics to elastometry. Further, obtained solutions are demonstrated to be rigorous benchmarks for testing coupled incompressible fluid–hyperelastic solid and multi-phase numerical solvers, towards which we highlight challenging parameter sets. Finally, we provide an interactive online sandbox to build physical intuition, and open-source our code-base.

Key words: flow-structure interactions, elastic waves, general fluid mechanics

1. Introduction

We report analytical solutions of a minimal yet representative problem involving a visco-elastic solid material layer sandwiched between two fluid layers, in turn confined by two long planar walls that undergo oscillatory motion (figure 1). We are motivated by the ubiquity and relevance of coupled interactions between viscous fluid and visco-elastic solids in engineering and biology (Dowell & Hall 2001; Grotberg & Jensen 2004; Heil & Hazel 2011; Zhu & Jane Wang 2011; Barthes-Biesel 2016). Despite the numerous efforts to investigate this class of systems across modalities (theory, simulations, experiments) and applications, from vesicle transport (Pozrikidis 2003; Vlahovska & Gracia 2007),

† Email address for correspondence: mgazzola@illinois.edu

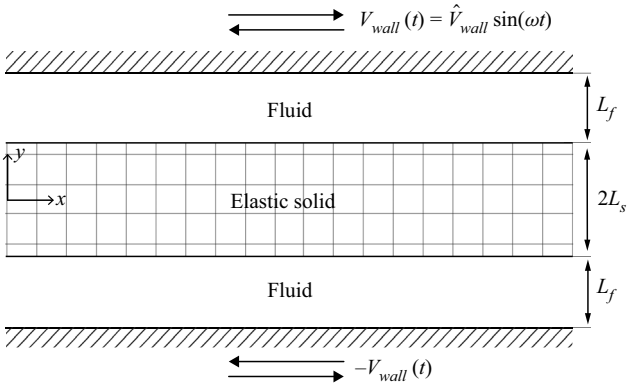

Figure 1. Schematic of the problem set-up.

pulmonary (Grotberg & Jensen 2004; Heil, Hazel & Smith 2008), oesophageal (Kou *et al.* 2017) or cardiovascular systems (Li, Vlahovska & Karniadakis 2013; Bodnár, Galdi & Nečasová 2014), biolocomotion (Argentina, Skotheim & Mahadevan 2007; Gazzola, Argentina & Mahadevan 2015; Tytell *et al.* 2016), microfluidics (Wang & Christov 2019; Christov 2021), drag reduction or energy harvesting (Alben, Shelley & Zhang 2002, 2004; Argentina & Mahadevan 2005; Bhosale *et al.* 2020), there is a perhaps surprising paucity of rigorous, analytical benchmarks that capture, in a minimal setting, tightly coupled, interfacially driven dynamics between elastic solids and shearing fluids. Such solutions are important to characterize system dynamics, relevant spatio-temporal scales, non-dimensional parameters and solution sensitivity, which are necessary for building intuition into practical flow–structure interaction problems.

Our set-up, inspired by Sugiyama *et al.* (2011), caters to these requirements by coupling an incompressible Newtonian fluid to an incompressible, density-mismatched visco-elastic solid using a single, well-defined interface. By analysing the flow field at this interface, the degree of dynamic coupling and underlying mechanisms can be understood. This analysis is possible because in our set-up, the governing equations reduce to the simplest possible case of a single dimension, while satisfying identically constraints of incompressibility. This results in decoupled algebraic equations that we solve to derive rigorous analytical solutions. These solutions help to isolate the spatio-temporal scales at play, and study the system behaviour across a range of physical conditions.

Insights may be relevant in a variety of practical settings. For example, in pusatile flows, bacterial deposition can be modulated through soft coatings (Bakker *et al.* 2003; Song, Koo & Ren 2015), offering avenues for controlling bio-film formation and preventing bio-fouling. Then our model may inform strategies for the manipulation of flow stresses through elastic surfaces (Gad-el Hak 2002). Similarly, our study may connect to the mechanics and wear of loaded synovial joints (Dowson & Jin 1986; Sun, Nalim & Yokota 2003; Nalim *et al.* 2004; Sun 2010), where wall-driven, cyclic (synovial) fluid shear stresses act on soft articular cartilages. Finally, our results may find use in non-destructive testing of solid rheological properties, much like Couette visco- and elasto-meters (Carr, Shen & Hermans 1976).

Within this context, we begin by providing a detailed derivation of the flow solution, first in the case of a solid modelled using a linear Kelvin–Voigt material. This established model captures the essence of visco-elasticity, by considering effectively a linear elastic

spring and viscous damper connected in parallel, and has proven insightful in minimal settings (Sengul 2021*a*,*b*). We first show how the obtained solution, in the limit of zero solid elastic shear modulus, is consistent with classical multi-phase Stokes–Couette flow solutions (Landau & Lifshitz 1987; Sim 2006; Leclaire *et al.* 2014). We then investigate the parametric impact of solid elasticity and fluid viscosity, and provide intuition for the observed results, using wave and boundary layer theory. During these parametric explorations, we discover regimes marked by solid displacements as high as four times that of the wall's oscillation amplitudes, which we attribute to elastic, standing wave harmonics. We then carry forth our analysis from linear Kelvin–Voigt solids to nonlinear Kelvin–Voigt solids, where elastic forces are modelled using a nonlinear spring, introduced here to approximate elastomeric and biological tissue responses (Bower 2009). Mathematically, the consequence is that closed-form solutions are no longer available. Thus to gain intuition, we turn to a numerical solution, which we then analyse.

Finally, our set-up also serves as a useful benchmark for validating fluid–elastic structure interaction and multi-phase simulation codes, towards which we highlight challenging parameter sets, compare with direct numerical simulations (Bhosale, Parthasarathy & Gazzola 2021), and provide an interactive online sandbox as well as open-source code.

The work is organized as follows. The problem set-up and governing equations are introduced in § 2. Simplifications and analytical solutions for linear Kelvin–Voigt solids are discussed in § 3, with the corresponding system behaviour presented in § 4. Numerical solutions for nonlinear Kelvin–Voigt solids and their interpretation are presented in § 5. Concluding remarks are provided in § 6.

2. Problem set-up and governing equations

A schematic of the set-up is shown in figure 1, where we have a two-dimensional (2-D) visco-elastic solid sandwiched between two layers of fluid, such that the system is top-down symmetric. The thicknesses of the solid and each fluid layer are $2L_s$ and L_f, respectively. The set-up is infinitely long, hence we assume homogeneity in the x-direction. The fluid is bounded by two planar walls that present a prescribed sinusoidal oscillatory motion $V_{wall}(t) := \hat{V}_{wall}\sin(\omega t) = \mathrm{Im}[\hat{V}_{wall}\exp(\mathrm{i}\omega t)]$, where hatted quantities denote the Fourier coefficients obtained upon a temporal Fourier transform, ω is the angular frequency of oscillations, and $T = 2\pi/\omega$ is the time period of oscillation. The bottom wall oscillates out of phase with the top wall, with phase shift π.

2.1. *Governing equations*

We consider a 2-D domain Σ occupied physically by elastic solid and viscous fluid, with Ω_e and $\partial\Omega_e$ representing the support and boundaries of the elastic solid, respectively. The fluid region is represented by $\Sigma - \bar{\Omega}$.

Linear and angular momentum balance in both the elastic solid and fluid phases, in the fixed lab frame of reference and on a continuum scale, leads to the Cauchy momentum equation

$$\frac{\partial \boldsymbol{v}}{\partial t} + \boldsymbol{\nabla}\cdot(\boldsymbol{v}\otimes\boldsymbol{v}) = -\frac{1}{\rho}\boldsymbol{\nabla}p + \frac{1}{\rho}\boldsymbol{\nabla}\cdot\boldsymbol{\sigma}', \quad \boldsymbol{x}\in\Sigma, \tag{2.1}$$

where $t\in\mathbb{R}^+$ represents time, $\boldsymbol{v}:\Sigma\times\mathbb{R}^+\to\mathbb{R}^2$ represents the velocity field, ρ denotes material density, $p:\Sigma\times\mathbb{R}^+\to\mathbb{R}$ represents the mean normal stress field

(i.e. thermodynamic pressure), and $\boldsymbol{\sigma}' : \Sigma \times \mathbb{R}^+ \to \mathbb{R}^2 \otimes \mathbb{R}^2$ stands for the deviatoric Cauchy stress tensor field. Throughout this work, the prime symbol $'$ on a tensor $\boldsymbol{A}$ indicates its deviatoric, i.e. $\boldsymbol{A}' := \boldsymbol{A} - \frac{1}{2}\,\mathrm{tr}(\boldsymbol{A})\,\boldsymbol{I}$, where $\boldsymbol{I}$ stands for the identity tensor, and $\mathrm{tr}(\cdot)$ represents the trace operator. All fields defined above are assumed to be sufficiently smooth in time and space. Additionally, incompressibility of the fluid and elastic domains results in the kinematic constraint on the velocity field

$$\boldsymbol{\nabla} \cdot \boldsymbol{v} \equiv 0, \quad \boldsymbol{x} \in \Sigma. \tag{2.2}$$

Interactions between the fluid and elastic solid phases take place via interfacial boundary conditions, which correspond to continuity in velocities (no-slip) and traction forces at the fluid–elastic solid interface:

$$\boldsymbol{v} = \boldsymbol{v}_f = \boldsymbol{v}_e, \quad \boldsymbol{n} \cdot \boldsymbol{\sigma}_f \cdot \boldsymbol{n} = \boldsymbol{n} \cdot \boldsymbol{\sigma}_e \cdot \boldsymbol{n}, \quad \boldsymbol{n} \cdot \boldsymbol{\sigma}_f \cdot \boldsymbol{t} = \boldsymbol{n} \cdot \boldsymbol{\sigma}_e \cdot \boldsymbol{t}, \quad \boldsymbol{x} \in \partial\Omega_e, \quad (2.3a\text{–}c)$$

where $\boldsymbol{n}$ and $\boldsymbol{t}$ denote the unit outward (solid to fluid) normal vector and the unit tangent vector at the interface $\partial\Omega_e$, respectively. Here, $\boldsymbol{v}_f$ and $\boldsymbol{v}_e$ correspond to the interfacial velocities in the fluid and the elastic body, respectively, while $\boldsymbol{\sigma}_f = -p\boldsymbol{I} + \boldsymbol{\sigma}_f'$ and $\boldsymbol{\sigma}_e = -p\boldsymbol{I} + \boldsymbol{\sigma}_e'$ correspond to the interfacial Cauchy stress tensors in the fluid and the elastic body, respectively.

2.2. *Simplification of governing equations*

We first simplify the governing equations by noting that the problem is homogeneous in the x-direction, hence we can omit the x-dependence of any quantity. The problem then reduces to one dimension, with gradients only along the y-axis, and classical symmetry reductions to the governing Cauchy momentum equation can be adopted. First, the continuity equation (or equivalently the incompressibility condition) of (2.2) simplifies to

$$\frac{\partial v^{[y]}}{\partial y} \equiv 0, \tag{2.4}$$

where the superscript indicates the directional component. A trivial solution of this equation is $v^{[y]}(y, t) = c(t)$, where $c(t)$ is an arbitrary quantity. Because of the absence of motion of the wall in the y-direction, $c(t)$ is identically zero to match wall boundary conditions. Then only the displacement $u^{[x]}(y, t)$, velocity $v^{[x]}(y, t)$ and stresses $\sigma^{[xy]}$ need to be considered. We remark that the thermodynamic pressure p in $\sigma^{[xy]}$ has zero gradient due to our assumption of homogeneity, hence we need to consider only deviatoric stresses $\sigma'^{[xy]}$. This simplifies the governing equation (2.1) in both the fluid (indicated by the subscript f) and solid (indicated by the subscript s) domain, yielding

$$\rho\, \partial_t v_j = \partial_y \sigma_j, \quad j = \{f, s\}, \qquad \text{where } \partial_t u_j = v_j, \tag{2.5}$$

where all quantities depend on (y, t), and the symbols $^{[\cdot]}$ and $'$ are dropped. In order to achieve closure of (2.5), we need to specify the form of internal material stresses, i.e. the constitutive relations. In this work, we assume the fluid to be Newtonian, isotropic and incompressible, with density ρ_f, dynamic viscosity μ_f, and kinematic viscosity $\nu_f = \mu_f/\rho_f$. Accordingly, the Cauchy stress is assumed to be

$$\sigma_f = \mu_f\, \partial_y v_f \quad (L_s \leqslant |y| < L_s + L_f). \tag{2.6}$$

The simplified equations (2.5) and (2.6) in the fluid indicate that accelerations (left-hand side) result from viscous forces alone.

Next, we assume that the solid is isotropic and incompressible, and is of constant density ρ_s and of nonlinear Kelvin-Voigt type, exhibiting visco-elastic behaviour. Then the Cauchy stress is assumed to be

$$\sigma_s = 2c_1\,\partial_y u_s + 4c_3\,(\partial_y u_s)^3 + \mu_s\,\partial_y v_s \quad (0 \leqslant |y| < L_s), \tag{2.7}$$

where μ_s represents the dynamic viscosity of the solid phase, and c_1, c_3 are coefficients of elastic moduli. This model, while unable to capture the full complexity of generalized nonlinear visco-elasticity, is well established as a minimal model and has been employed previously (Sengul 2021*a*,*b*) to gain insight into more general nonlinear visco-elastic phenomena. From this model, in the limit of zero solid viscosity $\mu_s = 0$, we recover the generalized Mooney–Rivlin constitutive model (Bower 2009; Sugiyama *et al.* 2011), appropriate to capture elastomeric and biological tissue responses. Here, in the infinitesimal deformations limit, the entity $2c_1$ represents G, the elastic shear modulus of the solid. In addition, setting $c_3 = 0$ in (2.7) implies linear stress responses with respect to the one-dimensional displacement u_s, while $c_3 \neq 0$ is responsible for (cubic) nonlinear behaviours (Sugiyama *et al.* 2011). Then setting $c_3 = 0$ and $2c_1 = G$ results in the Cauchy stress of a linear Kelvin–Voigt solid. Finally, similar to the fluid phase, we define the kinematic viscosity of the solid as $\nu_s = \mu_s/\rho_s$. Equations (2.5) and (2.7) indicate that accelerations (left-hand side) result from a combination of viscous and elastic forces in the solid (right-hand side).

Further, the stresses and velocities at the interfaces need to be continuous per (2.3), thus

$$\left.\begin{aligned} v_f(\pm L_s, t) &= v_s(\pm L_s, t), \\ \mu_f\,\partial_y v_f(\pm L_s, t) &= 2c_1\,\partial_y u_s(\pm L_s, t) + 4c_3\,(\partial_y u_s(\pm L_s, t))^3 + \mu_s\,\partial_y v_s(\pm L_s, t). \end{aligned}\right\} \tag{2.8}$$

Finally, we close the equations above by imposing no-slip boundary conditions at the upper and lower walls at $y = \pm(L_s + L_f)$:

$$v_f = \begin{cases} \hat{V}_{wall}\sin\omega t & \text{at } y = L_f + L_s, \\ -\hat{V}_{wall}\sin\omega t & \text{at } y = -(L_f + L_s). \end{cases} \tag{2.9}$$

In the case of a linear Kelvin–Voigt solid ($c_3 = 0$), the governing equations (2.5)–(2.9) reduce to a set of linear equations since our set-up involves purely shearing motions. We take two distinct, but equivalent, solution approaches. The first involves solving directly the linear governing equations in the physical domain. The second approach instead solves the modal form of the governing equations obtained via a sine transform. The first, closed-form solution is possible only in the linear Kelvin–Voigt case, while the second, infinite series solution can handle arbitrary constitutive models. We discuss both in the following.

3. Derivation of analytical solutions for linear Kelvin–Voigt solids

3.1. *Direct analytical solution*

The first approach, for a linear Kelvin–Voigt solid (with $c_3 = 0$), is to solve directly (2.5)–(2.7) in the fluid and solid domains. We begin by noting that due to symmetry, (2.5) can admit only solutions that are odd functions of y. Indeed, the equations of motion are invariant upon replacing $u(y, t)$, $v(y, t)$ with $-u(-y, t)$, $-v(-y, t)$ in both solid and fluid.

Thus we consider only solutions for $y \geqslant 0$ henceforth. Given $c_3 = 0$, we have

$$\left.\begin{aligned} \rho_f\, \partial_t v_f &= \mu_f\, \partial_y^2 v_f && \text{for fluid } (L_s \leqslant y < L_s + L_f), \\ \rho_s\, \partial_t^2 u_s &= 2c_1\, \partial_y^2 u_s + \mu_s\, \partial_y^2 \partial_t u_s && \text{for solid } (0 \leqslant y < L_s). \end{aligned}\right\} \tag{3.1}$$

Considering the linearity of (3.1), the symmetry of our set-up, and the sinusoidal form of wall velocity $V_{wall}(t) = \mathrm{Im}[\hat{V}_{wall} \exp(\mathrm{i}\omega t)]$, one can expect similar sinusoidal forms in resulting solid displacements $u_s(y, t) = \mathrm{Im}[\hat{u}_s(y) \exp(\mathrm{i}\omega t)]$ and flow velocities $v_f(y, t) = \mathrm{Im}[\hat{v}_f(y) \exp(\mathrm{i}\omega t)]$. Substituting these ansatzes in (3.1) yields

$$\left.\begin{aligned} \left(\partial_y^2 - \frac{\mathrm{i}\omega}{\nu_f}\right) \hat{v}_f &= 0 && \text{for fluid } (L_s \leqslant y < L_s + L_f), \\ \left(\partial_y^2 + \frac{\omega^2}{\mathrm{i}\omega\nu_s + (2c_1/\rho_s)}\right) \hat{u}_s &= 0 && \text{for solid } (0 \leqslant y < L_s), \end{aligned}\right\} \tag{3.2}$$

which are a pair of homogeneous Helmholtz equations with exact solutions

$$\left.\begin{aligned} \hat{v}_f(\tilde{y}) &= A \exp\left(k_f \frac{\tilde{y}}{L_f}\right) + B \exp\left(-k_f \frac{\tilde{y}}{L_f}\right), && \tilde{y} \in [0, L_f), \\ \hat{u}_s(y) &= C \exp\left(k_s \frac{y}{L_s}\right) + D \exp\left(-k_s \frac{y}{L_s}\right), && y \in [0, L_s), \end{aligned}\right\} \tag{3.3}$$

where $\tilde{y} = y - L_s$, and

$$k_f = \sqrt{\mathrm{i}}\,(L_f^{-1}(\nu_f/\omega)^{1/2})^{-1}, \quad k_s = \mathrm{i}[((\omega L_s)^{-1}(2c_1/\rho_s)^{1/2})^2 + \mathrm{i}(L_s^{-1}(\nu_s/\omega)^{1/2})^2]^{-1/2}. \tag{3.4a,b}$$

The coefficients A, B, C, D are determined directly given interface and boundary conditions (2.8) and (2.9), and their (lengthy) expressions are reported in § 1 of the supplementary material available at https://doi.org/10.1017/jfm.2022.542. Physically, (3.3) indicates a damped wave behaviour, in both solid and fluid domains.

3.2. *Modal solution using Fourier series*

The second approach, based on Sugiyama *et al.* (2011), consists in representing $u_s(y, t)$, $v_f(y, t)$ as Fourier sine series in the spatial coordinate y, injecting them into the governing equations (2.5)–(2.7), and matching the interfacial conditions of (2.8) and boundary conditions of (2.9) to obtain the final solutions. The choice of a sine series expansion is natural here given the Dirichlet velocity boundary conditions. Because of the piecewise definition of stresses in (2.6) and (2.7), and the interfacial condition in (2.8) (which indicates that velocities are $\mathcal{C}^0$ continuous), convergence can be poor if a global Fourier series (i.e. for both the solid and fluid domains together) is considered. Hence, we utilize two piecewise Fourier series expansions for the solid $v_s(y, t)$ and fluid $v_f(y, t)$ velocities, respectively, and impose explicitly $\mathcal{C}^0$ continuity in velocities and stresses. Then, due to symmetry, one can expand $u_s(y, t)$, $v_f(y, t)$ using the Fourier sine series

only in the upper half-space $y \geqslant 0$, as follows:

$$\left.\begin{aligned} v_f(\tilde{y}, t) &= V_I(t) + \frac{\tilde{y}}{L_f}\left(V_{wall}(t) - V_I(t)\right) + \sum_{k=1}^{\infty} v_{f,k}(t) \sin\frac{\pi k \tilde{y}}{L_f}, \\ u_s(y, t) &= \frac{U_I(t)\, y}{L_s} + \sum_{k=1}^{\infty} u_{s,k}(t) \sin\frac{\pi k y}{L_s}, \end{aligned}\right\} \tag{3.5}$$

where $U_I(t)$, $V_I(t)$ are the displacement and velocity of the solid–fluid interface at $y = L_s$, and $v_{f,k}(t)$ and $u_{s,k}(t)$ are the Fourier expansion coefficients of v_f and u_s, respectively. This expansion satisfies the incompressibility condition (2.2), odd symmetry requirement about $y = 0$, interfacial velocity conditions (2.8), and boundary velocity conditions (2.9) imposed in the set-up. Additional details regarding the expansion can be found in § 2 of the supplementary material. We also note that the interface displacement U_I and modal displacement $u_{s,k}$ satisfy

$$\frac{\mathrm{d}U_I}{\mathrm{d}t} = V_I, \quad \frac{\mathrm{d}u_{s,k}}{\mathrm{d}t} = v_{s,k}. \tag{3.6a,b}$$

Substituting the Fourier series defined in (3.5) into the governing equation (2.5), and utilizing the stress relations of (2.6) and (2.7), we rewrite the equations with all terms moved to the left-hand side:

$$\left.\begin{aligned} &\frac{\mathrm{d}V_I}{\mathrm{d}t} + \frac{\tilde{y}}{L_f}\left(\frac{\mathrm{d}V_{wall}}{\mathrm{d}t} - \frac{\mathrm{d}V_I}{\mathrm{d}t}\right) + \sum_{k=1}^{\infty}\left\{\frac{\mathrm{d}v_{f,k}}{\mathrm{d}t} + \nu_f\left(\frac{\pi k}{L_f}\right)^2 v_{f,k}\right\}\sin\frac{\pi k\tilde{y}}{L_f} = 0, \\ &\frac{y}{L_s}\frac{\mathrm{d}V_I}{\mathrm{d}t} + \sum_{k=1}^{\infty}\left\{\frac{\mathrm{d}^2 u_{s,k}}{\mathrm{d}t^2} + \nu_s\left(\frac{\pi k}{L_s}\right)^2\frac{\mathrm{d}u_{s,k}}{\mathrm{d}t} + \frac{2c_1}{\rho_s}\left(\frac{\pi k}{L_s}\right)^2 u_{s,k} + \frac{\pi k}{\rho_s L_s}\sigma_{NL,k}\right\}\sin\frac{\pi k y}{L_s} = 0, \end{aligned}\right\} \tag{3.7}$$

where $\nu_s = \mu_s/\rho_s$ and $\nu_f = \mu_f/\rho_f$ are the kinematic viscosities of the solid and fluid phases, respectively. Here, σ_{NL} denotes the nonlinear contribution (i.e. the term containing c_3) in the solid stress equation (2.7) with respect to the displacement, so that its expansion coefficients read

$$\sigma_{NL} := 4c_3\left(\frac{\partial u_s}{\partial y}\right)^3 = \sum_{k=0}^{\infty}\sigma_{NL,k}\cos\frac{\pi k y}{L_s}. \tag{3.8}$$

We then project the governing equations in physical space (3.7) onto the Fourier modal bases, and use Fourier identities (supplementary material § 3) to simplify the obtained expressions:

$$\frac{2}{\pi k}\left\{\frac{\mathrm{d}V_I}{\mathrm{d}t} - (-1)^k\frac{\mathrm{d}V_{wall}}{\mathrm{d}t}\right\} + \frac{\mathrm{d}v_{f,k}}{\mathrm{d}t} + \nu_f\left(\frac{\pi k}{L_f}\right)^2 v_{f,k} = 0, \tag{3.9}$$

$$-\frac{2(-1)^k}{\pi k}\frac{\mathrm{d}V_I}{\mathrm{d}t} + \frac{\mathrm{d}^2 u_{s,k}}{\mathrm{d}t^2} + \nu_s\left(\frac{\pi k}{L_s}\right)^2\frac{\mathrm{d}u_{s,k}}{\mathrm{d}t} + \frac{2c_1}{\rho_s}\left(\frac{\pi k}{L_s}\right)^2 u_{s,k} + \frac{\pi k}{\rho_s L_s}\sigma_{NL,k} = 0, \tag{3.10}$$

with $k = 1, \ldots, \infty$. In modal space, the continuity condition of shear stresses at the interface, upon substituting (3.5) into (2.8) and using the Fourier identities of

supplementary material § 3, reads

$$\frac{\mu_f(V_{wall}-V_I)}{L_f}-\frac{2c_1U_I}{L_s}-\sigma_{NL,0}$$
$$-\frac{\mu_sV_I}{L_s}\sum_{k=1}^{\infty}\left[\frac{\mu_f\pi k v_{f,k}}{L_f}-(-1)^k\left\{\frac{2c_1\pi k u_{s,k}}{L_s}+\frac{\mu_s\pi k}{L_s}\frac{\mathrm{d}u_{s,k}}{\mathrm{d}t}+\sigma_{NL,k}\right\}\right]=0. \quad (3.11)$$

Equations (3.9)–(3.11) relate directly the modal expansion coefficients $v_{f,k}$ in the fluid, and $u_{s,k}$ in the solid, via the interfacial quantities U_I, V_I as functions of the physical set-up parameters. We now need to solve (3.9)–(3.11) for the modal quantities $v_{f,k}, u_{s,k}$ and interfacial quantities U_I, V_I. To do so, we truncate the number of modes in the above infinite Fourier series to $k = K - 1$. This leads to a truncation error, which we minimize by taking K to be large. Here, K is fixed to 1024 unless otherwise indicated.

We now specialize the above solutions for the linear Kelvin–Voigt case with $c_3 = 0$. First, similar to § 3.1, we expect sinusoidal forms for the temporal quantities

$$V_I(t)=\mathrm{Im}[\hat{V}_I\exp(\mathrm{i}\omega t)],\quad v_{f,k}(t)=\mathrm{Im}[\hat{v}_{f,k}\exp(\mathrm{i}\omega t)],\quad u_{s,k}(t)=\mathrm{Im}[\hat{u}_{s,k}\exp(\mathrm{i}\omega t)]. \quad (3.12a\text{–}c)$$

Substitution of the temporal transformed quantities from (3.12*a–c*) in the momentum ODEs (3.9) and (3.10) leads to algebraic equations that can be solved. Upon algebraic manipulation and taking into account the modal stress balance (3.11), we obtain

$$\hat{u}_{s,k}=-\frac{\mathrm{i}(-1)^k\hat{V}_I\beta_k}{\pi\omega k},\quad \hat{v}_{f,k}=\frac{\{(-1)^k\hat{V}_{wall}-\hat{V}_I\}\alpha_k}{\pi k}, \quad (3.13a,b)$$

where $\hat{V}_I, \alpha_k, \beta_k$ are coefficients whose expressions are tedious and hence deferred to supplementary material § 4. The expressions of (3.13*a*,*b*) can then be used directly in (3.5) to evaluate solid displacements, fluid velocities and solid velocities. This provides the final modal solution for the case of a linear Kelvin–Voigt solid.

Our solution approaches are equivalent and generate the same results (supplementary material § 5). Having discussed both these approaches, we now identify key non-dimensional quantities that characterize the system physically, validate our solutions against known special cases and direct numerical simulations, analyse parametric behaviour, and investigate implications on the system response.

4. Analysis of system behaviour for linear Kelvin–Voigt solids

4.1. *Key driving parameters*

The proposed system can be characterized fully through a set of non-dimensional parameters, deduced from our solutions above, which are listed in table 1. Here, the Reynolds number *Re* captures the importance of inertial effects in the fluid phase using the ratio of inertial to viscous forces. Higher *Re* indicates an inertia-dominated response from the fluid. The Ericksen number *Er* captures the importance of elasticity in the solid phase using the ratio of viscous to elastic forces. Lower *Er* indicates an elasticity-dominated response from the solid. The fluid Stokes layer thickness δ_f captures the boundary layer length scale associated with the exponential decay of wall velocity, relative to the fluid layer thickness. Low values of δ_f indicate significant decay of wall velocity in the fluid. The solid Stokes layer thickness δ_s has a similar interpretation, but for the solid. The elastic

Symbol	Definition	Physical interpretation
L	$2(L_s + L_f)$	Length scale
L_f/L_s		Length ratio
$\dot{\gamma}$	$2\hat{V}_{wall}/\omega L$	Non-dimensional shear rate
Re	$\dot{\gamma}\omega L_f^2/\nu_f$	Reynolds number
Er	$\mu_f\dot{\gamma}\omega/2c_1$	Ericksen number
ρ	ρ_s/ρ_f	Density ratio
ν	ν_s/ν_f	Viscosity ratio
δ_f	$L_f{}^{-1}(\nu_f/\omega)^{1/2} = \exp(\mathrm{i}\pi/4)\,k_f^{-1} = \left(\dfrac{\dot{\gamma}}{Re}\right)^{1/2}$	Non-dimensional fluid Stokes layer thickness
δ_s	$L_s{}^{-1}(\nu_s/\omega)^{1/2} = \sqrt{\mathrm{Im}[-k_s^{-2}]} = (L_f/L_s)\left(\dfrac{\nu\dot{\gamma}}{Re}\right)^{1/2}$	Non-dimensional solid Stokes layer thickness
λ	$(\omega L_s)^{-1}(2c_1/\rho_s)^{1/2} = \sqrt{Re[-k_s^{-2}]} = (L_f/L_s)\left(\dfrac{\dot{\gamma}^2}{\rho\, Re\, Er}\right)^{1/2}$	Non-dimensional elastic wavelength

Table 1. Characteristic non-dimensional parameters.

wavelength λ captures the length scale associated with elastic shear waves progressing from the interface into the solid bulk, relative to the solid layer thickness. Low values of λ indicate high elastic wavenumbers within the solid phase. The relevance of these length scales δ_f, δ_s, λ will become apparent as we discuss the system response in § 4.2.

In this work, we fix the geometry $L_s = L_f = L/4$, and unless stated otherwise, we assume non-dimensional shear rate $\dot{\gamma} = \pi^{-1}$ and density ratio $\rho = 1$. We remark that these assumptions do not affect the generality of our results. Indeed, the effects of $\dot{\gamma}$, ρ can be reproduced through fluid viscosity ν_f and solid elasticity c_1, via the non-dimensional parameters of table 1.

Having defined the key non-dimensional parameters, we can now investigate their impact on the behaviour of the system.

4.2. *Limit cases*

In order to develop a physical intuition for the system response, we first remove selectively the effects of solid viscosity ($\nu_s \to 0$) and elasticity ($c_1 \to 0$), and analyse our solution. In these limit cases, we recover classical analytical results.

4.2.1. *Purely elastic solid case ($\nu_s = 0$)*

In the limit of $\nu_s = 0$, the solid is purely elastic (with a neo-Hookean constitutive model) and we recover the solution of Sugiyama *et al.* (2011) (up to minor typographical errors in that work). Here we consider the set-up shown in figure 2 with parameters taken from Sugiyama *et al.* (2011), to enable comparison with their results. This system is characterized by $Re = 0.25$, $Er = 1/(5\pi)$, $\nu = 0$, $\delta_f = 1.12$, $\delta_s = 0$, $\lambda = 2.52$, where $\nu = \nu_s/\nu_f$ is the viscosity ratio.

We begin our comparison by highlighting representative non-dimensional velocity profiles obtained from our solutions. We showcase profiles only in the upper half-plane, shown in figure 2(*a*), due to symmetry in our set-up. We plot the profiles corresponding to the marked line station in figure 2(*a*), at different time instants (or equivalently phases) within one oscillation cycle. These profiles are presented in figure 2(*b*), with colours

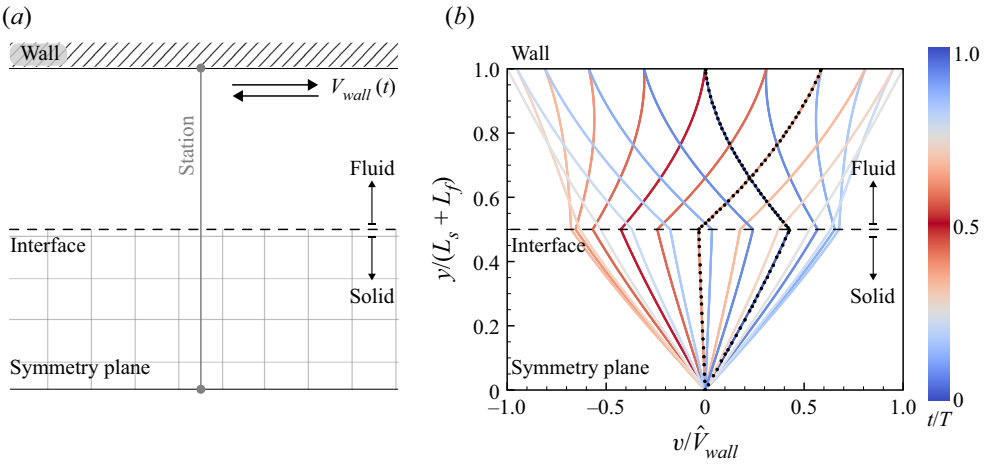

Figure 2. Pure elastic solid limit. Non-dimensional velocity profiles in y for a pure elastic solid (with a neo-Hookean constitutive model). The system response is shown only in the upper half-plane. The system is characterized by $Re = 0.25$, $Er = 1/(5\pi)$, $\nu = 0$, $\delta_f = 1.12$, $\delta_s = 0$, $\lambda = 2.52$, where $\nu = \nu_s/\nu_f$ is the viscosity ratio. Additional details can be found in supplementary material § 6. The same set of parameters is analysed in Sugiyama *et al.* (2011), whose profiles (provided at only two time instants) are overlaid as black scatter points on our curves. Colours represent t/T.

indicating time instants. For reference, the wall is located at $y/(L_s + L_f) = 1$, and the symmetry plane is located at $y/(L_s + L_f) = 0$. The interface is located at $y/(L_s + L_f) = 0.5$, below which we have the elastic solid zone, and above which we have the fluid zone. In this plot we also overlay the velocity profiles (black points) predicted by Sugiyama *et al.* (2010). While they provide profile data for only two time instants, we find favourable agreement with our velocity profiles, at both times. From these velocity profiles, we see that the solid velocity exhibits a phase lag (indicated by the colours) relative to the fluid velocity, and less pronounced magnitudes. The fluid's maximum velocity magnitude always occurs at the wall ($|v| = \hat{V}_{wall}$), while the solid velocity magnitudes always reach a minimum at the symmetry plane ($|v| = 0$). Finally, the slopes of the velocity profiles $\partial_y v$ are discontinuous at the interface, to satisfy continuity in stresses (2.8).

We can gain an intuition for these profiles by considering force balance in the fluid and solid phases separately. That is, at any point in space–time, the sum of all real and apparent (i.e. inertial acceleration) forces must add up to zero. In the viscous fluid, we have inertial and viscous contributions, as seen from $-\partial_t v + \nu\, \partial_y^2 v = 0$. This balance equation indicates that viscous forces operate by acting on the curvature $\partial_y^2 v$ of the velocity profile. Thus both high viscosity ν (low Re) and high velocity profile curvature $\partial_y^2 v$ contribute to increasing viscous forces, which then balance out accelerations exactly. Typically, these viscous forces (and velocity profile curvatures) are concentrated within a boundary layer close to the wall (seen from the structure of the solution in (3.3)), characterized by the non-dimensional Stokes layer thickness δ_f. Within this boundary layer, viscous forces cause the flow velocity to decay rapidly before eventually reaching the interface.

From the moving interface (no-slip), the solid phase displacement propagates into the bulk, mediated by elastic forces. From (2.5)–(2.7), the elastic contribution to solid force balance is $-\partial_t v + 2c_1\, \partial_y^2 u = 0$. This indicates that elastic forces operate by acting on the curvature $\partial_y^2 u \propto \omega^{-1}\, \partial_y^2 v$ of the solid velocity profile v. So both high elastic shear modulus

$2c_1$ (low Er) and high velocity profile curvature $\partial_y^2 v$ contribute to increasing elastic forces. These elastic forces propagate as waves within the solid ($\nu_s = 0$, so λ_2 from (3.4*a*,*b*) is purely imaginary, leading to sinusoids in (3.3)), characterized by the non-dimensional elastic wavelength λ. This implies that a wave profile can be expected for velocities (and curvatures) within the solid, which then always adjusts to zero at the symmetry plane in a fashion similar to nodes in stationary waves. Additionally, for a visco-elastic solid ($\nu_s \neq 0$), we have viscous effects that set up a boundary layer close to the interface and symmetry planes, similar to the fluid phase. The extent of this region is characterized by the non-dimensional solid Stokes layer thickness δ_s.

Overall, across both fluid and solid phases, we can rationalize the observed velocity profiles by considering Re, Er and the curvature length scales $\delta_f, \delta_s, \lambda$. Referring back to figure 2, since $Re = 0.25 \sim O(1)$, we expect inertial and viscous forces to be approximately equally important in the fluid. Additionally, $\delta_f = 1.12 > 1$ indicates that the boundary layer occupies most of the fluid zone. This leads to moderate velocity curvatures throughout the fluid phase, as seen in figure 2(*b*). This, in turn, drives the solid phase characterized by no viscosity and low Er, indicating stiff/strong elastic behaviour. As a consequence of low Er, the wavelength $\lambda \propto Er^{-1/2}$ is large ($\lambda = 2.52 > 1$). We then expect to see only the nascent part of a wave, which is almost linear, as indeed is observed in figure 2(*b*).

4.2.2. *No elastic solid ($c_1 = 0$): single-phase and multi-phase Stokes–Couette flows*

Our solution recovers classical results in the limit of $c_1 = 0$, which indicates absence of elastic forces in the solid phase. Thus only viscous forces operate in the solid, effectively rendering it a Newtonian fluid. If $c_1 = 0$, $\mu_s = \mu_f = \mu$ and $\rho_s = \rho_f = \rho$, then the entire domain is occupied by a single fluid, and we recover the Stokes–Couette flow solution (Landau & Lifshitz 1987) valid throughout the domain. If instead $c_1 = 0$, but $\mu_s \neq \mu_f$ or $\rho_s \neq \rho_f$, then the domain is occupied by two different fluids, and we recover the multi-phase Stokes–Couette flow for two immiscible liquids, which has established piecewise analytical solutions (Sim 2006; Leclaire *et al.* 2014). Upon comparison with single- and double-phase Stokes–Couette flow references, our analytical formulations (§§ 3.1 and 3.2) are found in excellent agreement (see supplementary material § 7).

4.3. *Linear Kelvin–Voigt solid: verification against numerical simulations*

We now move on from analyses of limit cases and consider the more general scenario of visco-elastic linear Kelvin–Voigt solids. Before studying the system behaviour in a range of conditions (§ 4.4), we validate our solutions against direct numerical simulations (DNS) employing a recent 2-D remeshed vortex method framework (Bhosale *et al.* 2021). In figure 3(*a*), we consider a system characterized by $Re = 2$, $Er = 1$, $\nu = 0.1$, $\delta_f = 0.4$, $\delta_s = 0.126$, $\lambda = 0.225$. In these conditions $Re, Er \sim O(1)$, so that we expect elastic, viscous and inertial forces to be equally important in the solid, marking a departure from the above limit cases. Additionally, since $\lambda < 1$, we expect the emergence of wave-like profiles inside the solid. As illustrated in figure 3(*a*), our analytical solutions within the solid indeed exhibit a standing-wave-like behaviour, constrained by boundary layer adjustments (with characteristic high curvatures) near both the interface and the symmetry plane. These results are confirmed by DNS, as illustrated in figure 3(*c*), where we report the numerically obtained velocity profiles along the line-station of figure 3(*b*), overlaid

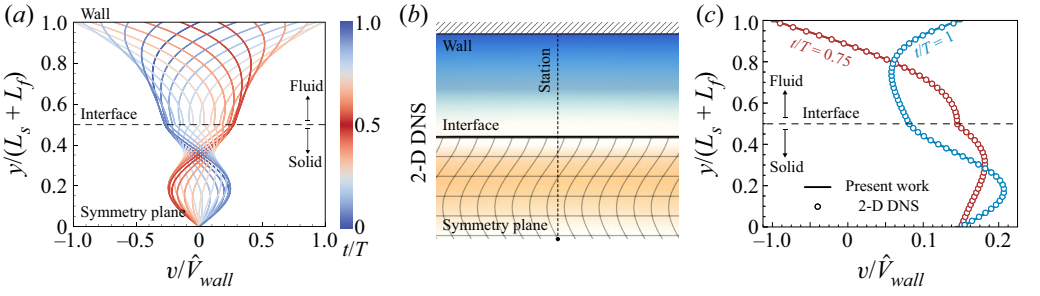

Figure 3. Comparison against simulations. (*a*) Non-dimensional analytical velocity profiles in y, for a visco-elastic solid with a neo-Hookean constitutive model. The system response is shown only in the upper half-plane. This system is characterized by $Re = 2$, $Er = 1$, $\nu = 0.1$, $\delta_f = 0.4$, $\delta_s = 0.126$, $\lambda = 0.225$. Additional details can be found in supplementary material § 6. Colours indicate t/T. (*b*) We solve the above problem through 2-D DNS (Bhosale *et al.* 2021) and run our simulations until the system reaches a dynamical steady state ($t/T = 10$), then sample quantities within the last cycle. Corresponding simulation parameters and set-up details can be found in supplementary material § 6. In the image, we mark the x-velocity field (orange/blue represent positive/negative velocity) and deformation contours within the solid, with the interface marked (black, thick solid) for visual clarity. (*c*) Upon plotting the velocity profiles at the highlighted station (black, dashed) in the centre of the domain, we see good agreement with our analytical results across all times. For the sake of clarity, we show profiles at only two different time instances. Here, numerical results are plotted with scatter points whereas analytical results are plotted with a solid line.

on the theoretical predictions. As can be seen, profiles compare favourably at multiple temporal instants, validating the accuracy of both our theory and the numerical solver.

4.4. *Range of soft, elastomeric interface dynamics*

Having validated our analytical solutions across different scenarios, we next investigate the dynamic response of the system for variations in the two most important parameters: elasticity (Er) and viscosity (Re). Here, we span the set of $Er = 0.1, 1, 10$, which includes the range of soft cellular tissue found in the human body (Wu *et al.* 2018; Guimarães *et al.* 2020), and $Re = 0.1, 0.5, 1, 2, 10$, which indicates small to moderate inertial effects. Our choices capture typical values found in oscillatory micro-fluidic assays and applications (highlighted in § 1) involving biological and soft elastomeric materials that operate in conjunction with fluid interfaces (Di Carlo 2009; Velve-Casquillas *et al.* 2010; Duncombe, Tentori & Herr 2015). Additional details on these parameter values can be found in supplementary material § 8.

Within this context, we focus on the system response (velocity profiles) first at low $Re = 0.1$ (figures 4*a–c*), then at (relatively) high $Re = 10$ (figures 4*m–o*) and finally at intermediate Re (figures 4*d–l*). For each Re, we consider the impact of Er, ranging from stiff (low Er, figures 4*a*,*d*,*g*,*j*,*m*) to soft solids (high Er, figures 4*c*,*f*,*i*,*l*,*o*). Within each Re regime, we discuss the fluid velocity profiles first, followed by the solid velocity profiles. Velocity profiles are rationalized using the length scales $\delta_f = (\dot{\gamma}\, Re)^{-1/2}$, $\delta_s = (\nu\dot{\gamma}/Re)^{1/2}$ and $\lambda = \dot{\gamma}\,(Re\, Er)^{-1/2}$, which are marked alongside each case study.

4.4.1. *Low Re*

First, at low $Re = 0.1$, we expect viscous forces to be important in the bulk flow. Indeed, the boundary layer in the fluid zone is characterized by $\delta_f \approx 1.8 > 1$, so that its thickness spans the entire flow domain. This thick boundary layer results in two prominent effects.

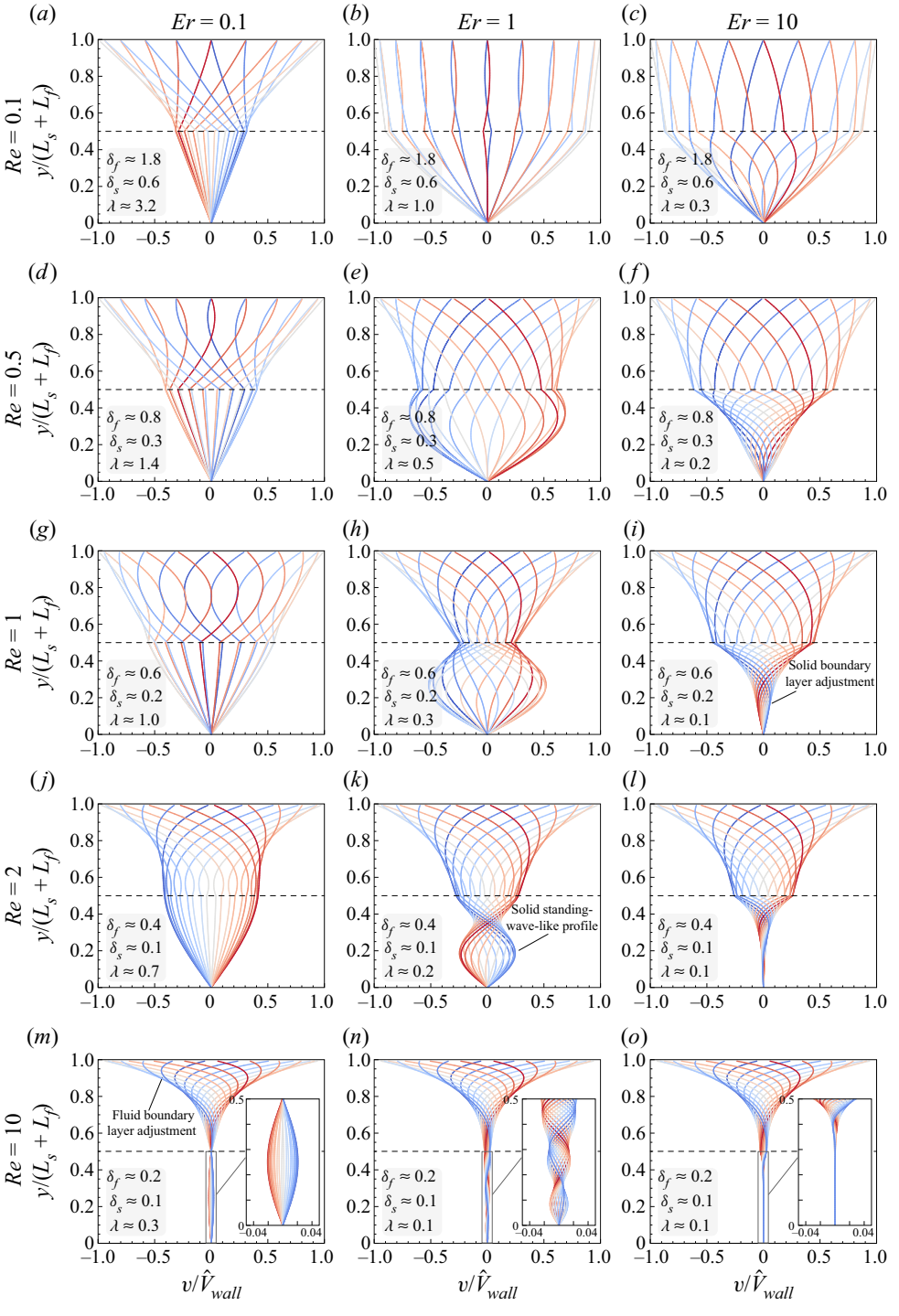

Figure 4. Dynamics with parametric variation. Non-dimensional velocity profiles in y for parametric changes in $Re = \{0.1, 0.5, 1, 2, 10\} \times Er = \{0.1, 1, 10\}$, with $\nu = 0.1$, $\rho = 1$. The system response is shown only for the upper half-plane, where we also mark the length scales δ_f, δ_s, λ. The black dashed lines indicate the solid–fluid interface. Colours represent t/T, with the same colour bar as in figure 2.

First, it indicates that fluid velocities have minimal curvature, which we confirm from figures 4(*a–c*). Second, it effectively transmits the viscous stresses induced by the wall to the interface, which then initiates motion in the bulk solid. At this low Re, the thickness $\delta_s \approx 0.6$ of the solid boundary layer spans the bulk of the solid domain itself. In addition, unlike the fluid phase, we now also have elastic contributions, which we investigate by spanning Er. At low $Er = 0.1$, the solid has a large elastic wavelength $\lambda \approx 3.2 > 1$. Hence, similar to § 4.2.1, we expect the velocity profiles to have no wave-like behaviour, and thus less curvature. This is confirmed by figures 4(*a*,*d*,*g*,*j*,*m*), where we see approximately linear solid velocity profiles, justified intuitively by the fact that to balance out acceleration forces, the elasticity modulus c_1 has to be large when curvatures are minimal (see § 4.2.1).

If we then increase Er, going from stiffer (figures 4*a*,*d*,*g*,*j*,*m*) to softer (figures 4*c*,*f*,*i*,*l*,*o*) solids, we expect both elastic and viscous forces to contribute equally to the dynamics. This is accompanied by decreasing values of λ, which indicate that more wavelengths can now fit in the solid layer thickness. Then, similar to § 4.3, we expect the appearance of standing-wave-like profiles, with prominent boundary layer adjustments close to interface and symmetry planes. These considerations are confirmed in figures 4(*a–c*), where we see that solid velocity profiles exhibit increasing curvatures as we move from left to right.

4.4.2. *Higher Re*

Next, for $Re = 10$, we see prominent boundary layer adjustments in the fluid close to the wall. This is due to the characteristically low boundary layer thickness $\delta_f \approx 0.2 < 1$, which implies that fluid velocity curvatures can be high only within this compact region. Indeed, beyond this boundary layer, the fluid velocity decays rapidly before reaching the interface, leading to the profiles shown in figures 4(*m–o*). As a result of this decay, the flow cannot effectively transmit viscous stresses to the interface, hence the solid barely deforms. This flow decay is dependent only on Re, so we expect similar small solid deformation amplitudes even if we vary the solid elasticity. We confirm this intuition by increasing Er (left to right), noticing small solid velocity amplitudes. Hence in this Re regime, the fluid evolves almost independently ('weak coupling') from the details of the solid. In contrast, the low Re regime seen earlier is 'strongly coupled'. Finally, we note that increasing Er, i.e. decreasing λ, leads to wavy profiles (although of small magnitude) inside the solid.

4.4.3. *Intermediate Re*

For intermediate Re, the system showcases a rich variety of behaviours, which we highlight by investigating parameters around $Re = 1$. First, in these cases the fluid's boundary layer has moderate thickness $\delta_f \sim O(1)$, hence we expect moderate velocity profile curvatures over δ_f. By decreasing δ_f (e.g. by increasing Re), we expect the flow curvature to increase. We confirm this in figure 4, as we move from $Re = 0.5$ (figures 4*a–c*) to $Re = 2$ (figures 4*m–o*). An increase in Re also increases the solid velocity curvatures, by decreasing both the solid wavelength λ and solid boundary layer thickness $\delta_s \sim O(0.1)$. The effect of decreasing λ is displayed prominently as we move from $Re = 0.5$ to $Re = 2$ for a fixed $Er = 1$ (figures 4*b*,*e*,*h*,*k*,*n*). Further, at high Er, we expect viscous forces to dominate over elastic forces, thus rendering the solid medium more fluid-like. Indeed, for $Er = 10$, the solid velocity profiles showcase a boundary layer adjustment similar to the one encountered in fluids. Hence, as we span Er from 0.1 to 10 at intermediate $Re = 0.5 - 2$, the effects of viscosity and elasticity compete in the solid leading

to rich dynamics. As a consequence, in this regime, solid velocity profiles are especially sensitive to changes in Er. Such sensitivity provides a potential mechanism to manipulate and control interfacial stress magnitudes in the previously mentioned applications. Finally, because of its dynamic variety and sensitivity, this intermediate parameter regime is identified as challenging numerically, therefore we propose the parameter sets $Re = \{0.5, 1, 2\}$ and $Er = \{0.1, 1, 10\}$ for benchmarking flow–structure interaction solvers, as illustrated in figure 3.

4.5. *Solid phase resonance*

We conclude this section by investigating the conditions under which resonant solid deformations may occur. These might serve well applications such as elastometry, where high-amplitude peaks can provide unique footprints to characterize materials.

We begin by defining the gain function $|G| \geqslant 0$ as the ratio of solid to wall amplitude which, from (3.3), is given by the closed-form expression

$$|G| = \left| \frac{\mathrm{i}\omega C}{\hat{V}_{wall}} \right| = \frac{2}{|(\mathrm{e}^{k_f - k_s} - \mathrm{e}^{-(k_f - k_s)})(1-\alpha) - (\mathrm{e}^{k_f + k_s} - \mathrm{e}^{-(k_f + k_s)})(1+\alpha)|}, \tag{4.1}$$

where k_f and k_s are the fluid and solid wave contributions (see (3.4*a*,*b*)), and $\alpha = (L_f/L_s)(k_s/k_f)(\rho\nu - \mathrm{i}(\dot{\gamma}/Er))$ captures the degree of fluid–solid coupling.

In the limit case of a purely elastic solid ($\nu = 0$), the denominator of G is always > 0, due to the non-zero contributions from the fluid phase ($k_f \neq 0$). The immediate implication is that unbounded resonance, $|G| \to \infty$, is not possible in our set-up because the fluid always dampens out high amplitudes in the solid phase. Thus interstitial fluids, besides providing lubrication as in synovial joints, may also prevent excessive deformations and subsequent failure of the soft, articular cartilage.

In figure 5(*a*), we plot $|G|$ as a function of Er, Re with $\nu = 0$. As can be seen, characteristic gain peaks ($|G| > 1$, bright yellow) take place and manifest as families of hyperbolae $Re\,Er = k^2$. Here, $k = \pi/\lambda$ corresponds to discrete harmonic wavenumbers with wavelength $\lambda = (\pi^2\, Re\, Er)^{-1/2}$, from table 1. Hence higher k corresponds to higher harmonics. To gain further intuition, we fix $Re = 1$ (chosen because of its dynamic richness, see figure 4), and plot $|G|$ versus Er to obtain the red curve of figure 5(*c*). We see four distinct high-gain peaks ⓪ – ③ of increasing amplitude, where the numbers represent the standing wave mode. In the cases ① – ③, the solid displaces more than the driving wall (figures 5*d–f*), with velocity profiles corresponding to the first three harmonics. Case ⓪ is characterized by the fact that maximal amplitudes occur at the interface, and not in the bulk, thus behaving as a standing wave with a free end at the interface.

Realistic materials include internal dissipation effects, which we enable here by adding viscosity to the solid. This reduces $|G|$ amplitudes, but preserves the hyperbolic structure of peaks, as seen in figure 5(*b*).

Finally, 2-D DNS simulations for $\nu = 0, 10^{-2}$ (black scatter points in figures 5*d*,*g*) validate our model predictions. Since it is challenging numerically to capture these high-gain regimes, we propose $Re = 1$, $Er = 1.3$, $\nu = 0, 10^{-2}$ for benchmarking numerical simulations, in addition to the parameter sets presented in § 4.4.

We have thus provided analytical solutions for the dynamics of a visco-elastic linear Kelvin–Voigt solid immersed in an oscillatory Couette flow system. We have derived a general solution to account for arbitrary solid densities and viscosities in our set-up,

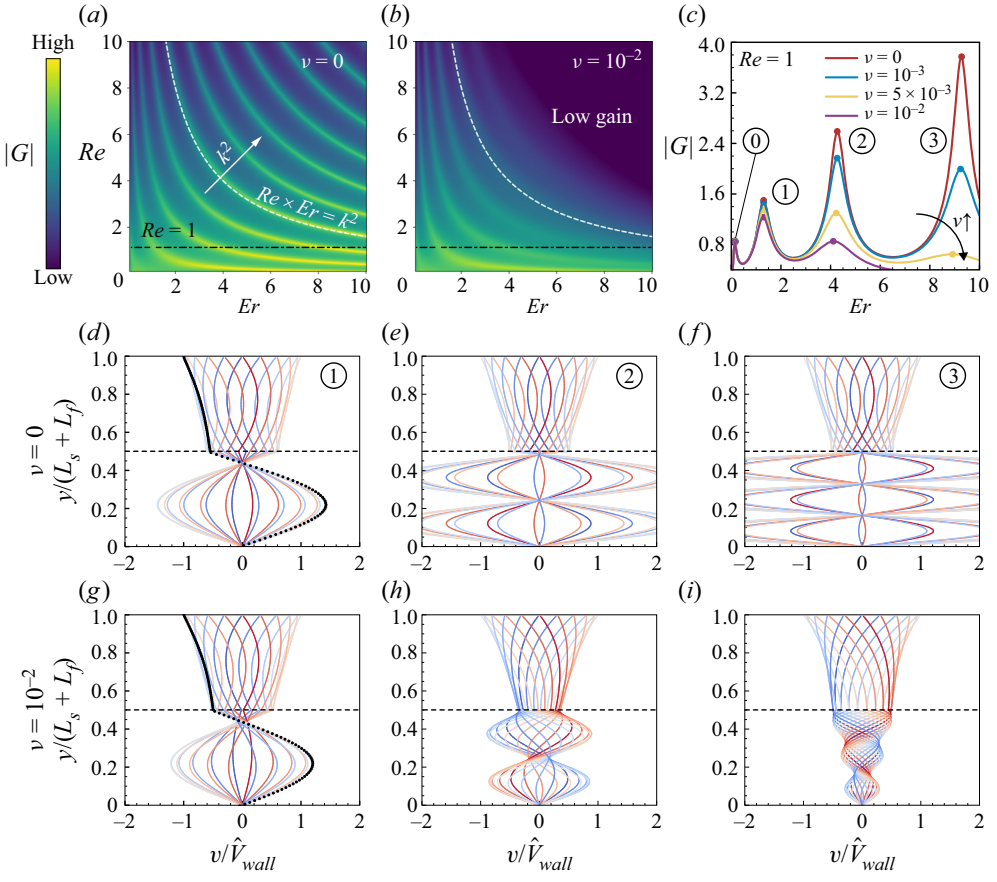

Figure 5. High amplitude gains. Phase map of $|G|$ as a function of Re, Er shows distinct regions of high (bright yellow) and low (dark blue) gains in cases with viscosity ratios (*a*) $\nu = 0$, (*b*) $\nu = 10^{-2}$, with maxima in both cases along $Re\,Er = k^2$ (white dashed line), where k increases in the direction of the arrow in (*a*). We fix $Re = 1$ and plot $|G|$ against Er along the black dashed line in (*a*) for different viscosity ratios ν (coloured) in (*c*), which shows four distinct peaks, ⓪ to ③, at $Er = 0.14, 1.3, 4.27, 9.27$. Increasing viscosity decreases $|G|$ peaks, especially for ② and ③. Plotting the velocity profiles corresponding to ① to ③ at $\nu = 0$ in (*d–f*) and $\nu = 10^{-2}$ in (*g–i*) reveals that they resemble harmonic standing waves within the solid. We confirm that these high-gain results are indeed physical by plotting equivalent 2-D DNS results as black scatter points in (*d*,*g*) where we notice agreement between the curves.

using two approaches – one in modal space generalizing the previous work of Sugiyama *et al.* (2011), and one in physical space. As a special limiting case, we recover the original solution of Sugiyama *et al.* (2011) for a density-matched solid with zero viscosity. Additionally, we recover analytical solutions of single-fluid (Landau & Lifshitz 1987) and multi-fluid (Sim 2006; Leclaire *et al.* 2014) Stokes–Couette flows in the limit of zero solid elastic shear modulus. Further, our solutions compare well against DNS results (figure 3). They are found to exhibit a range of behaviours (figure 4), including high gains (figure 5), with potential applications in biophysics and engineering. Next, we discuss the case of a nonlinear Kelvin–Voigt solid, which presents higher-order nonlinear effects within the solid.

5. Generalization to nonlinear Kelvin–Voigt solids

5.1. *Modal solutions*

In the case of a nonlinear Kelvin–Voigt solid, characterized by $c_3 \neq 0$, the elastic stress is proportional to the cubic power of strain (see (2.7)), which signifies a higher-order nonlinear response to deformations. The resulting equations, whose nonlinearity is captured overall via the parameter $c = c_3/c_1$, resist closed-form analytical solutions. Then, to investigate the system response in this setting, we derive a solution using the Fourier series machinery of § 3.2, which we then evaluate numerically.

The solution strategy here is to employ a Fourier pseudo-spectral collocation scheme (Sugiyama *et al.* 2011) for evaluating the nonlinear stress terms $\sigma_{NL,k}$ in the governing equation (3.10), at a finite set of grid points $x_j = (j + \frac{1}{2})\,\Delta x$, with $\Delta x = L_s/K$. All other terms are treated as described in § 3.2.

Armed with this spatial discretization, we employ a numerical time integration scheme to evolve the nonlinear equations (3.9) and (3.10). We use a second-order constant timestepper (of timestep Δt) comprised of mixed Crank–Nicolson (implicit, for stability in the viscous updates) and explicit Nyström (midpoint) rule for the second-order time derivatives (Hairer, Nørsett & Wanner 1991). If we denote the nth time level $t = n\,\Delta t$ by a superscript n, then the prescribed wall velocity takes the analytical form

$$V_{wall}^{(n+1)} := V_{wall}((n+1)\,\Delta t) = \mathrm{Im}[\hat{V}_{wall}\exp(\mathrm{i}\omega((n+1)\,\Delta t))]. \tag{5.1}$$

For the interface displacement U_I and fluid velocity update in (3.9), we use the Crank–Nicolson scheme (Hairer *et al.* 1991)

$$U_I^{(n+1)} \approx U_I^{(n)} + \frac{\Delta t}{2}\,(V_I^{(n+1)} + V_I^{(n)}) + O(\Delta t^2), \tag{5.2}$$

and for updating the interface velocity V_I and solid displacements in (3.10), we utilize the explicit Nyström (midpoint) rule

$$\left(\frac{\mathrm{d}V_I}{\mathrm{d}t}\right)^{(n)} \approx \frac{V_I^{(n+1)} - V_I^{(n-1)}}{2\,\Delta t} + O(\Delta t^2). \tag{5.3}$$

Upon substituting these discretizations in the governing equations (3.9) and 3.10, and by invoking the modal stress balance of (3.11) at every step, we obtain the solution, after standard (but tedious) algebraic manipulations. For brevity, we omit derivation details, which can be found in supplementary material § 9.

5.2. *Analysis of system behaviour*

We first validate our solutions against DNS (figure 6) in the set-up of figure 3, but with $c = 4$ instead of $c = 0$. The choice of c is consistent with established biological tissue models (Raghavan & Vorp 2000). As can be seen in figure 6(*a*), the solid velocity profiles exhibit characteristic high-curvature bends (marked), differently from the linear Kelvin–Voigt case (figure 3) on account of the additional material nonlinearity. Further, as illustrated in figure 6(*c*), our solutions are found to agree well with DNS.

Next, in the spirit of figure 4, we highlight system responses upon varying both degree of solid nonlinearity (c) and viscosity (Re). Throughout this exploration, we fix the elastic to viscous contributions by setting $Er = 1$ and $\nu = 0.1$. These values are informed by the rich dynamics of figures 4(*b*,*e*,*h*,*k*,*n*). We then choose values that

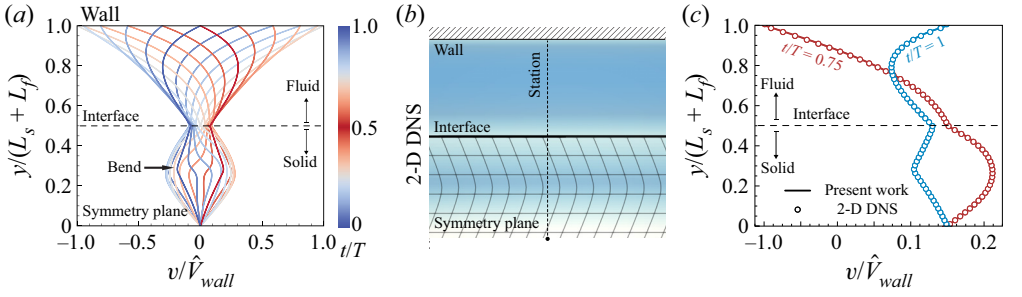

Figure 6. Comparison against simulations. (*a*) Non-dimensional velocity profiles in y, for a nonlinear Kelvin–Voigt solid. The system response is shown only in the upper half-plane. This system is characterized by $Re = 2$, $Er = 1$, $\nu = 0.1$, $c = c_3/c_1 = 4$, $\delta_f = 0.4$, $\delta_s = 0.126$, $\lambda = 0.225$. Additional details can be found in supplementary material § 6. Colours indicate t/T. We also mark a high curvature bend in the profile with a black arrow. (*b*) We solve the above problem through 2-D DNS (Bhosale *et al.* 2021) with corresponding simulation parameters reported in supplementary material § 6. In this image, we mark the x-velocity field (orange/blue represent positive/negative velocity) and deformation contours within the solid, with the interface marked (black, thick solid) for visual clarity. Upon plotting the velocity profiles at the highlighted station (black, dashed) in the centre of the domain, we see good agreement with our results across all times as shown in (*c*). For the sake of clarity, we show profiles at only two different time instances. Here, numerical results are plotted with scatter points, whereas present results are plotted with a solid line.

span $(c, Re) \in \{1, 5, 10\} \times \{0.1, 0.5, 1, 2, 10\}$, and report the responses of the system in figure 7.

For solids with small c, we expect dynamics similar to the linear Kelvin–Voigt counterpart. This is confirmed from the solid zone profiles in figures 7(*a*,*d*,*g*,*j*,*m*). Increasing the nonlinearity coefficient stiffens the solid, constraining deformation velocities (narrower envelopes) as well as producing sharper bends (marked), as we move from left to right in figure 7.

Changing viscosity (Re) affects the response in a fashion similar to the linear case (figure 4), where profile curvatures in both fluid and solid phases get concentrated progressively within sharper boundary layers, as we move from top to bottom in figure 7.

Finally, we investigate whether the high-gain regimes seen in § 4.5 exist for nonlinear Kelvin–Voigt solids, and if so, under what conditions. Here, unlike § 4.5, there is no mathematical guidance to identify high-gain parameters, thus we explore the Er–Re phase space numerically for the representative cases $c = 1$ (figure 8*a*) and $c = 5$ (figure 8*b*). For $c = 1$, we see in figure 8(*a*) that high-gain peaks (bright yellow) still occur in a regular structure, although they are less pronounced and depart from the hyperbolae seen in the linear Kelvin–Voigt case, now lying on the curve-fit $Re\,Er^{0.5} = const.$ In figure 8(*c*), we report the velocity profiles of a representative high-gain case, and note that $|v/\hat{V}_{wall}|$ hardly exceeds 1, as opposed to the linear Kelvin–Voigt cases of figure 5. As we increase c from 1 to 5, we observe that the peaks spread apart and lie on the curve-fit $Re\,Er^{0.4} = \text{const.}$, and gains diminish further (figure 8*b*). We conclude that the cubic term that characterizes nonlinear Kelvin–Voigt solids stiffens the material locally, reducing its propensity to deform and shear.

6. Conclusion

We have presented solutions for an oscillatory Couette set-up involving parallel visco-elastic solid–fluid layers sandwiched between two oscillating planar walls.

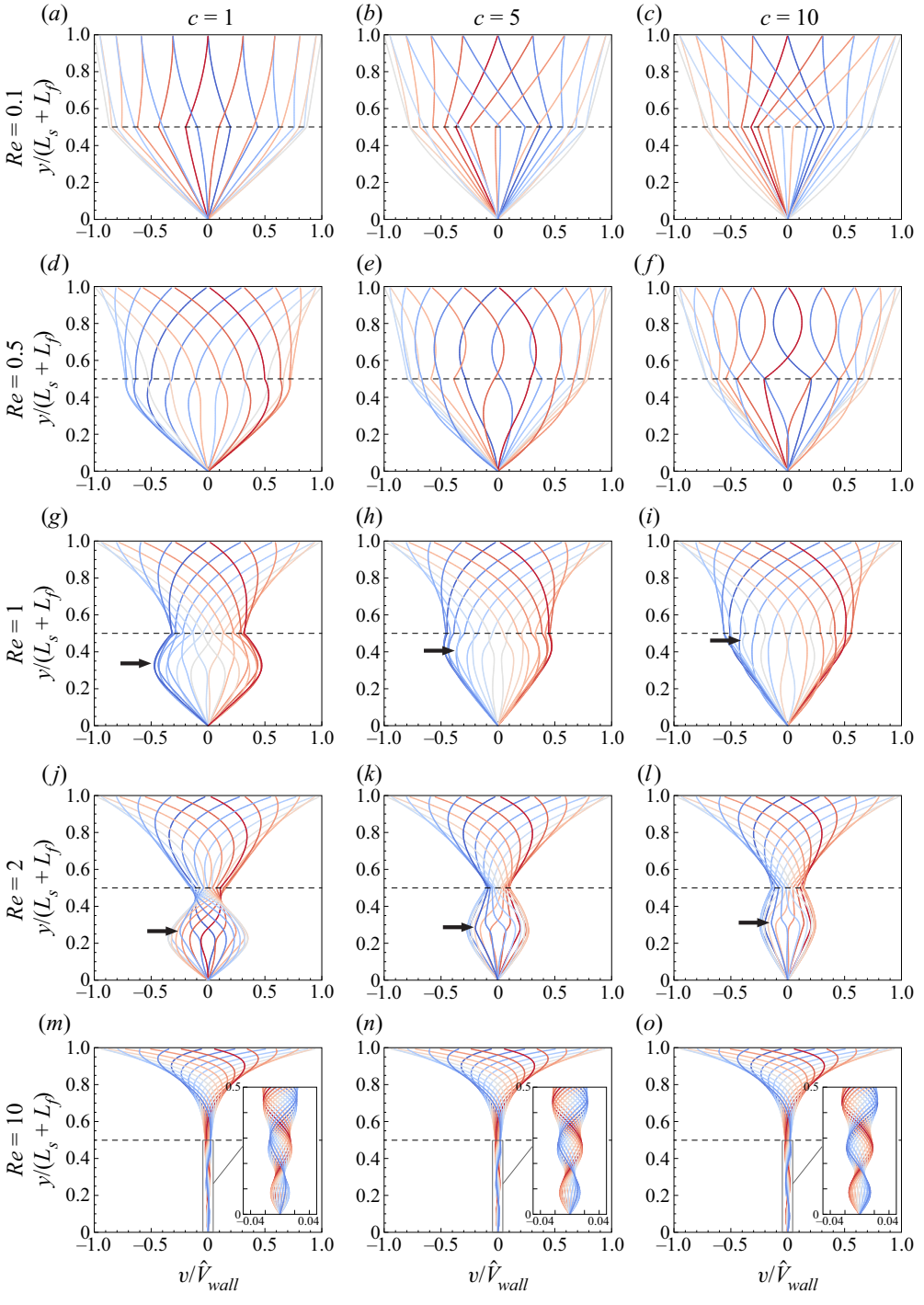

Figure 7. Dynamics with parametric variation. Non-dimensional velocity profile in y for parametric changes that span $(c, Re) \in \{1, 5, 10\} \times \{0.1, 0.5, 1, 2, 10\}$ with $Er = 1$, $\nu = 0.1$, $\rho = 1$. The system response is shown only in the upper half-plane. The black dashed lines indicate the solid–fluid interface. Colours represent t/T, with the same colour bar as in figure 2. We also mark the location of prominent high-curvature bends in the profiles with a black arrow.

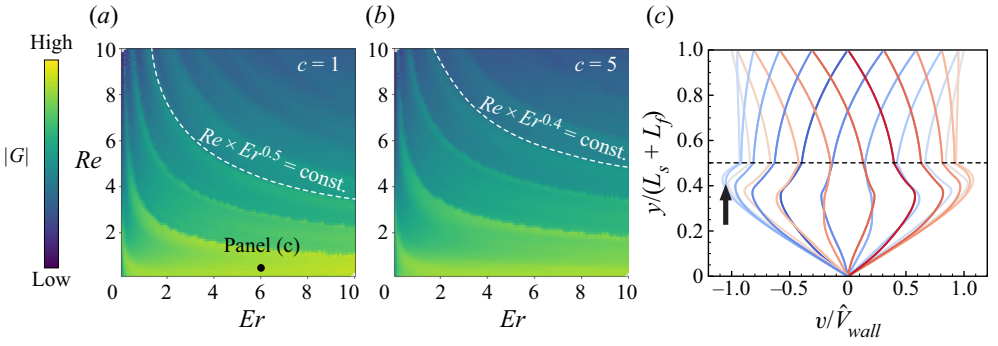

Figure 8. High amplitude gains for a nonlinear Kelvin–Voigt solid. Phase map of numerically measured $|G|$ as a function of Re, Er, for $\nu = 10^{-3}$ and (*a*) $c = 1$, (*b*) $c = 5$, shows regions of high (bright yellow) and low (dark blue) gains with maxima along $Re\,Er^{0.5} = \text{const.}$ and $Re\,Er^{0.4} = \text{const.}$, respectively, deviating from the hyperbolae seen in the linear Kelvin–Voigt case. The curves are obtained from a numerical fitting procedure, with details reported in supplementary material § 10. Velocity profiles of a representative case with $Re = 0.2$, $Er = 6$, $c = 1$ marked in (*a*) and plotted in (*c*) showcase high-gain bends (marked) characteristic of strong nonlinear effects in the solid.

We are motivated by the paucity of minimal yet representative elasto-hydrodynamicsystems that can be analysed analytically and rigorously, given their relevance and ubiquity in biophysical and engineering settings. Here, we consider visco-elastic solids with arbitrary density and viscosity immersed in a Newtonian fluid. We derive two equivalent analytical solutions for linear Kelvin–Voigt solids – one based on homogeneous Helmholtz equations, and another based on partitioned Fourier series expansions. For nonlinear Kelvin–Voigt solids, we turn to numerical solutions using a pseudo-spectral scheme. We leverage these solutions to deduce non-dimensional parameters, which we then employ to rationalize the system's rich dynamical repertoire over physically realistic parameter ranges. Our analysis connects to a number of practical biophysical scenarios ranging from bio-film/bio-fouling control to wear and tear of soft biological interfaces as in synovial joints. We further uncover regimes characterized by high solid phase displacements, attributed to standing wave harmonics, which serve as unique footprints to characterize the solid material. This provides a novel non-destructive approach for elastometry, never proposed before to the best of our knowledge. Altogether, our results provide a basis for developing intuition into coupled elasto-hydrodynamic systems, towards which we provide an interactive online sandbox (supplementary material § 11), and open-source our code.

Supplementary material. Supplementary material is available at https://doi.org/10.1017/jfm.2022.542.

Funding. The authors acknowledge support by the National Science Foundation under NSF CAREER grant no. CBET-1846752 (M.G.).

Declaration of interests. The authors report no conflict of interest.

Author ORCIDs.
Mattia Gazzola https://orcid.org/0000-0003-2129-379X.

References

Alben, S., Shelley, M. & Zhang, J. 2002 Drag reduction through self-similar bending of a flexible body. *Nature* **420** (6915), 479–481.

ALBEN, S., SHELLEY, M. & ZHANG, J. 2004 How flexibility induces streamlining in a two-dimensional flow. *Phys. Fluids* **16** (5), 1694–1713.

ARGENTINA, M. & MAHADEVAN, L. 2005 Fluid-flow-induced flutter of a flag. *Proc. Natl Acad. Sci.* **102** (6), 1829–1834.

ARGENTINA, M., SKOTHEIM, J. & MAHADEVAN, L. 2007 Settling and swimming of flexible fluid-lubricated foils. *Phys. Rev. Lett.* **99** (22), 224503.

BAKKER, D.P., HUIJS, F.M., DE VRIES, J., KLIJNSTRA, J.W., BUSSCHER, H.J. & VAN DER MEI, H.C. 2003 Bacterial deposition to fluoridated and non-fluoridated polyurethane coatings with different elastic modulus and surface tension in a parallel plate and a stagnation point flow chamber. *Colloids Surf.* B*: Biointerfaces* **32** (3), 179–190.

BARTHES-BIESEL, D. 2016 Motion and deformation of elastic capsules and vesicles in flow. *Annu. Rev. Fluid Mech.* **48**, 25–52.

BHOSALE, Y., ESMAILI, E., BHAR, K. & JUNG, S. 2020 Bending, twisting and flapping leaf upon raindrop impact. *Bioinspir. Biomim.* **15** (3), 036007.

BHOSALE, Y., PARTHASARATHY, T. & GAZZOLA, M. 2021 A remeshed vortex method for mixed rigid/soft body fluid–structure interaction. *J. Comput. Phys.* **444**, 110577.

BODNÁR, T., GALDI, G.P. & NEČASOVÁ, Š. 2014 *Fluid–Structure Interaction and Biomedical Applications*. Springer.

BOWER, A.F. 2009 *Applied Mechanics of Solids*. CRC Press.

CARR, M.E., SHEN, L.L. & HERMANS, J. 1976 A physical standard of fibrinogen: measurement of the elastic modulus of dilute fibrin gels with a new elastometer. *Analyt. Biochem.* **72** (1-2), 202–211.

CHRISTOV, I.C. 2021 Soft hydraulics: from Newtonian to complex fluid flows through compliant conduits. Preprint. arXiv:2106.07164.

DI CARLO, D. 2009 Inertial microfluidics. *Lab on a Chip* **9** (21), 3038–3046.

DOWELL, E.H. & HALL, K.C. 2001 Modeling of fluid–structure interaction. *Annu. Rev. Fluid Mech.* **33** (1), 445–490.

DOWSON, D. & JIN, Z.-M. 1986 Micro-elastohydrodynamic lubrication of synovial joints. *Engng Med.* **15** (2), 63–65.

DUNCOMBE, T.A., TENTORI, A.M. & HERR, A.E. 2015 Microfluidics: reframing biological enquiry. *Nat. Rev. Mol. Cell Biol.* **16** (9), 554–567.

GAD-EL HAK, M. 2002 Compliant coatings for drag reduction. *Prog. Aerosp. Sci.* **38** (1), 77–99.

GAZZOLA, M., ARGENTINA, M. & MAHADEVAN, L. 2015 Gait and speed selection in slender inertial swimmers. *Proc. Natl Acad. Sci.* **112** (13), 3874–3879.

GROTBERG, J.B. & JENSEN, O.E. 2004 Biofluid mechanics in flexible tubes. *Annu. Rev. Fluid Mech.* **36**, 121–147.

GUIMARÃES, C.F., GASPERINI, L., MARQUES, A.P. & REIS, R.L. 2020 The stiffness of living tissues and its implications for tissue engineering. *Nat. Rev. Mater.* **5** (5), 351–370.

HAIRER, E., NØRSETT, S.P. & WANNER, G. 1991 *Solving Ordinary Differential Equations I, Nonstiff Problems*. Springer.

HEIL, M. & HAZEL, A.L. 2011 Fluid–structure interaction in internal physiological flows. *Annu. Rev. Fluid Mech.* **43**, 141–162.

HEIL, M., HAZEL, A.L. & SMITH, J.A. 2008 The mechanics of airway closure. *Respir. Physiol. Neurobiol.* **163** (1-3), 214–221.

KOU, W., PANDOLFINO, J.E., KAHRILAS, P.J. & PATANKAR, N.A. 2017 Simulation studies of the role of esophageal mucosa in bolus transport. *Biomech. Model. Mechanobiol.* **16** (3), 1001–1009.

LANDAU, L.D. & LIFSHITZ, E.M. 1987 Fluid Mechanics. In *Theoretical Physics*, vol. 6, pp. 336–343. Pergamon.

LECLAIRE, S., PELLERIN, N., REGGIO, M. & TRÉPANIER, J.Y. 2014 Unsteady immiscible multiphase flow validation of a multiple-relaxation-time lattice Boltzmann method. *J. Phys.* A*: Math. Theor.* **47** (10), 105501.

LI, X., VLAHOVSKA, P.M. & KARNIADAKIS, G.E. 2013 Continuum- and particle-based modeling of shapes and dynamics of red blood cells in health and disease. *Soft Matt.* **9** (1), 28–37.

NALIM, R., PEKKAN, K., SUN, H.B. & YOKOTA, H. 2004 Oscillating Couette flow for *in vitro* cell loading. *J. Biomech.* **37** (6), 939–942.

POZRIKIDIS, C. 2003 *Modeling and Simulation of Capsules and Biological Cells*. CRC Press.

RAGHAVAN, M.L. & VORP, D.A. 2000 Toward a biomechanical tool to evaluate rupture potential of abdominal aortic aneurysm: identification of a finite strain constitutive model and evaluation of its applicability. *J. Biomech.* **33** (4), 475–482.

SENGUL, Y. 2021*a* Nonlinear viscoelasticity of strain rate type: an overview. *Proc. R. Soc.* A **477** (2245), 20200715.

SENGUL, Y. 2021*b* Viscoelasticity with limiting strain. *Discr. Contin. Dyn. Syst.-Ser.* S **14** (1), 57–70.

SIM, W.-G. 2006 Stratified steady and unsteady two-phase flows between two parallel plates. *J. Mech. Sci. Technol.* **20** (1), 125.

SONG, F., KOO, H. & REN, D. 2015 Effects of material properties on bacterial adhesion and biofilm formation. *J. Dental Res.* **94** (8), 1027–1034.

SUGIYAMA, K., II, S., TAKEUCHI, S., TAKAGI, S. & MATSUMOTO, Y. 2010 Full Eulerian simulations of biconcave neo-Hookean particles in a Poiseuille flow. *Comput. Mech.* **46** (1), 147–157.

SUGIYAMA, K., II, S., TAKEUCHI, S., TAKAGI, S. & MATSUMOTO, Y. 2011 A full Eulerian finite difference approach for solving fluid–structure coupling problems. *J. Comput. Phys.* **230** (3), 596–627.

SUN, H.B. 2010 Mechanical loading, cartilage degradation, and arthritis. *Ann. N.Y. Acad. Sci.* **1211** (1), 37–50.

SUN, H.B., NALIM, R. & YOKOTA, H. 2003 Expression and activities of matrix metalloproteinases under oscillatory shear in IL-1-stimulated synovial cells. *Connect. Tissue Res.* **44** (1), 42–49.

TYTELL, E.D., LEFTWICH, M.C., HSU, C.-Y., GRIFFITH, B.E., COHEN, A.H., SMITS, A.J., HAMLET, C. & FAUCI, L.J. 2016 Role of body stiffness in undulatory swimming: insights from robotic and computational models. *Phys. Rev. Fluids* **1** (7), 073202.

VELVE-CASQUILLAS, G., LE BERRE, M., PIEL, M. & TRAN, P.T. 2010 Microfluidic tools for cell biological research. *Nano Today* **5** (1), 28–47.

VLAHOVSKA, P.M. & GRACIA, R.S. 2007 Dynamics of a viscous vesicle in linear flows. *Phys. Rev.* E **75** (1), 016313.

WANG, X. & CHRISTOV, I.C. 2019 Theory of the flow-induced deformation of shallow compliant microchannels with thick walls. *Proc. R. Soc.* A **475** (2231), 20190513.

WU, P.-H., *et al.* 2018 A comparison of methods to assess cell mechanical properties. *Nat. Meth.* **15**, 491–498.

ZHU, D. & JANE WANG, Q. 2011 Elastohydrodynamic lubrication: a gateway to interfacial mechanics – review and prospect. *J. Tribol.* **133** (4), 041001.